Orbital order drives magnetic order in math xmlns="http://www.w3.org/1998/Math/MathML">mrow>mn>5/mn>msup>mi>d/mi>mn>1/mn>/msup>/mrow>/math> and math xmlns="http://www.w3.org/1998/Math/MathML">mrow>mn>5/mn>msup>mi>d/mi>mn>2/mn>/msup>/mrow>/math> double perovskite Mott insulators

Christopher Svoboda, Wenjuan Zhang, Mohit Randeria, and Nandini Trivedi

Phys. Rev. B **104**, 024437 — Published 29 July 2021

DOI: 10.1103/PhysRevB.104.024437

Orbital order drives magnetic order in $5d^1$ and $5d^2$ double perovskite Mott insulators

Christopher Svoboda,[1] Wenjuan Zhang,[1] Mohit Randeria,[1] and Nandini Trivedi[1]

[1] *Department of Physics, The Ohio State University, Columbus, Ohio 43210, USA*

(Dated: July 13, 2021)

We derive spin-orbital Hamiltonians for cubic double perovskite $A_2MM'O_6$ Mott insulators with $5d^1$ or $5d^2$ magnetic M′ ions and non-magnetic M ions. We find that strong spin-orbit coupling, exchange and inter-site Coulomb repulsion lead to orbital order at a temperature T_o higher than the magnetic T_c. Orbital order produces a T-dependent moment below T_o and stabilizes canted ferromagnetic (FM) and non-collinear antiferromagnetic (AFM) states below T_c. We explain many experimental puzzles including loss of entropy above T_c, deviations from a Curie-Weiss susceptibility, a negative Curie-Weiss intercept for FM systems, and why FM order is common in cubic $5d^1$ materials but all $5d^2$ systems are AFM.

Introduction: The interplay between spin-orbit coupling (SOC) and strong correlations has provided a new platform to study exotic phases of matter, including quantum spin liquids and topological semimetals.[1,2] It is thus important to better understand the nature of orbital and magnetic interactions and the resulting broken symmetries, or lack thereof, in $4d$ and $5d$ transition metal oxides, before understanding their topological properties. While iridiates with $5d^5$ configuration have received a great deal of attention,[2] other fillings realized in oxides of Re and Os are much less studied.

We focus here on cubic double perovskites $A_2MM'O_6$, with magnetic M′ ions in the $5d^1$ or $5d^2$ configuration and non-magnetic M. These materials are Mott insulators as large separation between M′ ions on the FCC lattice leads to a small bandwidth relative to the on-site Coulomb repulsion. As we shall see, in the presence of strong SOC, exchange and inter-site Coulomb repulsion lead to an unusual orbital ordering onsets at a high temperature, which strongly constrains the magnetic interactions and the nature of the magnetic ordering.

Puzzles: Our work is motivated by the following puzzles:
(1) Why is there a predominance of FM order in cubic $5d^1$ double perovskites, but no known examples of ferromagnetism in $5d^2$ double perovskites? For instance, the $5d^2$ compounds Ca_3OsO_6[3], Ba_2CaOsO_6[4], and Sr_2MgOsO_6[5,6] all exhibit AFM order. Many $5d^1$ (undistorted) cubic systems, such as Ba_2NaOsO_6[7], Ba_2ZnReO_6[8], and Ba_2MgReO_6[8] are FM, with the possible exception of Ba_2LiOsO_6[7] which is cubic and AFM.
(2) In $5d^1$ materials, the single electron in the t_{2g} orbitals is in a $j=3/2$ state with 4 degenerate levels. Why then is the entropy recovered across the magnetic transitions in cubic compounds, e.g., Ba_2NaOsO_6[9] and Ba_2MgReO_6[8], only $R\ln 2$ and not $R\ln 4$?
(3) There are several puzzling features in the magnetic susceptibility χ of $5d^1$ materials above T_c, which are not understood. First, its high temperature behavior deviates strongly from the Curie-Weiss (CW) form $\chi(T) = \mu_{\rm eff}^2/[3k_B(T-\Theta)]$ in some materials[8]. Second, when the CW form does fit the data over a temperature range, the extracted $\Theta < 0$, characteristic of AFM interactions, even though $\chi(T)$ diverges at $T_c > 0$ below which FM order develops; e.g. in Ba_2NaOsO_6[9], Ba_2MgReO_6[8], and Ba_2ZnReO_6[8].

Previous works on $5d^1$ or $5d^2$ double perovskites have used density functional theory (DFT)[10–14] and model Hamiltonian approaches[15–19]. Our work builds on refs.[15,16] to address the finite temperature issues highlighted above that have not been addressed earlier; we discuss below the differences between our results and earlier works; see also Appendix A.

Main results: We derive an effective spin-orbital Hamiltonian for double perovskite systems and based on a mean field analysis we find the following:
(a) Orbital ordering occurs at T_o that is always higher than the magnetic T_c independent of choice of parameters. We note that orbital ordering in the L-S basis is essentially equivalent to quadrupolar order in the J-basis. While T_o is determined by both inter-site, orbital-dependent Coulomb repulsion V and superexchange interactions, only the latter determines the scale of T_c.
(b) The full recovery of entropy $R\ln 4$ does not occur at the magnetic T_c, but only above the orbital transition T_o.
(c) The onset of orbital order leads to T-dependent orbital occupancies, and thus a T-dependent effective moment $\mu_{\rm eff}(T)$. This is the origin of the strong deviations from CW behavior in the high T susceptibility.
(d) The orbital order determines the nature of magnetic interactions that are frustrated on an FCC lattice. This stabilizes non-collinear magnetic order. For d^1 systems, a canted FM state dominates in the large SOC limit, though a 4-sublattice AFM state is also possible in a small parameter regime.
(e) For d^2 systems, the occupied-to-occupied AFM superexchange pathways dominate over the occupied-to-empty FM superexchange, stabilizing AFM phases.

d^1 Systems: We focus on the t_{2g} orbitals of the M′ ions. The Hamiltonian has four terms, the first of which describes the electronic structure in the t_{2g} manifold:

$$H_{\rm TB} = -t\sum_{\alpha}\sum_{\langle ij\rangle\in\alpha}\sum_{\sigma} c^{\dagger}_{i,\alpha,\sigma}c_{j,\alpha,\sigma} + \text{h.c.}. \qquad (1)$$

Here $\langle ij\rangle$ denotes nearest-neighbor (NN) M′ sites, σ labels spin and the orbital index $\alpha \in \{yz, zx, xy\}$ also labels planes in the FCC lattice of M′'s, since electrons in

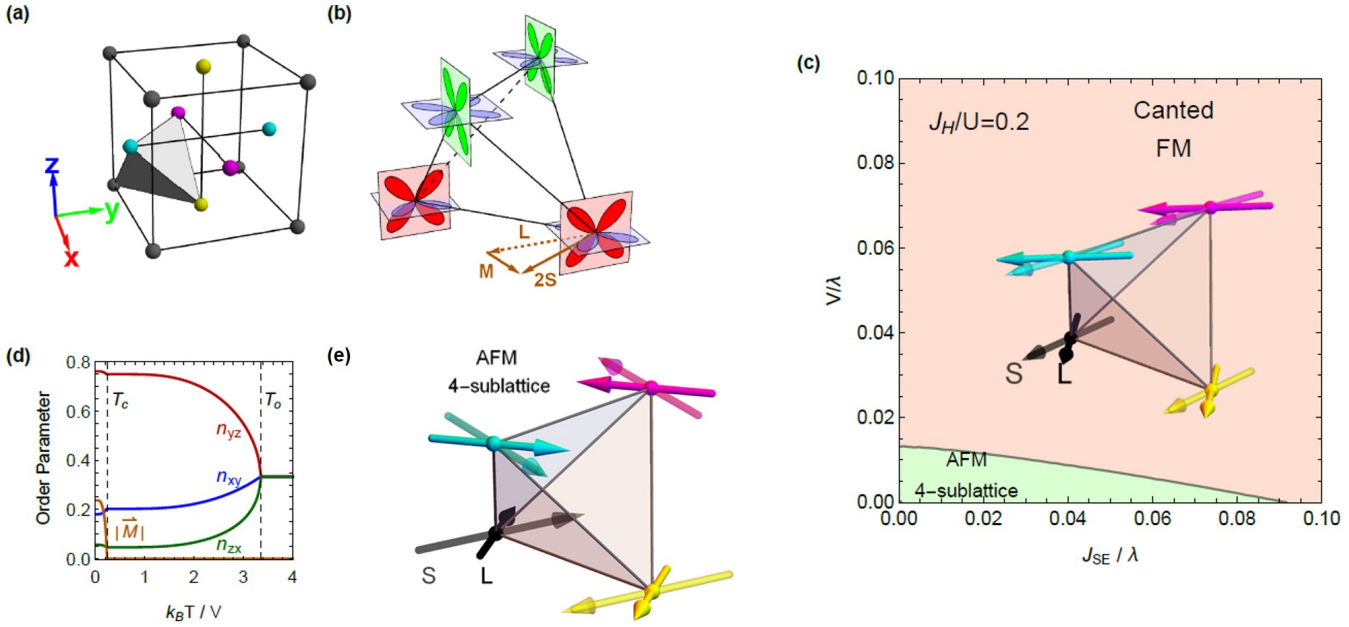

FIG. 1. (a) FCC lattice with four sites used in our mean field theory shown by four different colors. (b) Orbital ordering for d^1 systems driven by V and $J_{\rm SE}$. Orbitals with the largest (smaller) occupancy are in solid (lighter) colors; the lowest occupancy orbital is not shown. Orbital order constrains the orientation (but not the sign) of $\pm\boldsymbol{L}$. The magnetization $\boldsymbol{M}=2\boldsymbol{S}-\boldsymbol{L}$ is also shown. (c) The $T=0$ phase diagram: The orbital $\boldsymbol{L}$ (solid arrows) and spin $\boldsymbol{S}$ moments (semi-transparent arrows) are collinear in each plane, but rotated by $\simeq 90^\circ$ between planes, due to the orbital ordering pattern. (d) Orbital occupancies as a function of temperature for $J_{\rm SE}=V=\lambda/20$ for the black and yellow sites. The n_{yz} orbital (red) has the largest occupancy followed by the xy orbital (blue) and then zx (green). (e) $\boldsymbol{L}$ and $\boldsymbol{S}$ moments in the 4-sublattice AFM state.

xy orbitals hop only in the xy plane, and similarly for other corresponding planes. Second, the multi-orbital on-site Coulomb interaction $H_{\rm U}=\sum_i H_{\rm U}^{(i)}$, with

$$H_{\rm U}^{(i)}=(U-3J_H)\tfrac{1}{2}N_i(N_i-1)+J_H\left(\tfrac{5}{2}N_i-2\boldsymbol{S}_i^2-\tfrac{1}{2}\boldsymbol{L}_i^2\right) \quad (2)$$

where U is the Coulomb repulsion and J_H is Hund's coupling[20]. Third, the unquenched t_{2g} orbital angular momentum $l=-1$ results in SOC: $H_{\rm SO}=-\lambda\sum_i \boldsymbol{L}_i\cdot\boldsymbol{S}_i$. Fourth, the large spatial extent of $5d$ orbitals leads to inter-site Coulomb repulsion

$$H_{\rm V}=V\sum_\alpha\sum_{\langle ij\rangle\in\alpha}\left[\tfrac{9}{4}n_i^\alpha n_j^\alpha-\tfrac{4}{3}(n_i^\beta-n_i^\gamma)(n_j^\beta-n_j^\gamma)\right], \quad (3)$$

in the electric quadrupole approximation[15]. Here the orbital occupation $n_i^\alpha=\sum_\sigma c^\dagger_{i,\alpha,\sigma}c_{i,\alpha,\sigma}$. The interaction depends on the relative directionality between neighboring orbitals, e.g., a pair of xy orbitals in the xy-plane repel each other more than an xy and yz orbital.

Using parameter estimates[9,10] of the the hopping (between NN M′ sites in $A_2MM'O_6$) $t\simeq 50-100$ meV and the Coulomb interaction $U\simeq 3$ eV, we see that we are in a Mott regime ($U\gg t$). A strong coupling expansion of $H_{\rm TB}+H_{\rm U}$ leads to the superexchange (SE) Hamiltonian

$$H_{\rm SE}=-\frac{J_{\rm SE}}{4}\sum_\alpha\sum_{\langle ij\rangle\in\alpha}\Big\{r_1(\tfrac{3}{4}+\boldsymbol{S}_i\cdot\boldsymbol{S}_j)(n_i^\alpha-n_j^\alpha)^2 +(\tfrac{1}{4}-\boldsymbol{S}_i\cdot\boldsymbol{S}_j)\left[r_2(n_i^\alpha+n_j^\alpha)^2+\tfrac{4}{3}(r_3-r_2)n_i^\alpha n_j^\alpha\right]\Big\} \quad (4)$$

where $J_{\rm SE}=4t^2/U$ and the strength of Hund's coupling is characterized by $r_1=(1-3\eta)^{-1}$, $r_2=(1-\eta)^{-1}$, $r_3=(1+2\eta)^{-1}$ with[21] $\eta=J_H/U$. The first line of Eq. (4) describes FM spin interactions when one of the two orbitals is occupied while the other is unoccupied. The second line of (4) describes an AFM spin interaction that is maximized when both orbitals are singly occupied. J_H/U determines the relative strength of these two interactions. Additionally, there is an effective orbital repulsion $n_i^\alpha n_j^\alpha$ for $J_H\neq 0$.

The low-energy effective Hamiltonian is $H_{\rm eff}=H_{\rm SO}+H_{\rm V}+H_{\rm SE}$, whose largest energy scales is the SOC $\lambda\sim 0.4$ eV for $5d$ oxides[22,23] The SE $J_{\rm SE}\sim 10$ meV using $t\sim 100$ meV and $U\sim 3$ eV. J_H/U is known[24] to be $\simeq 0.2$. The inter-site repulsion V is not known reliably but could be comparable to or larger than SE.[25]

We find it is useful to work in the L-S basis, rather than projecting down to the $j=3/2$ subspace. This gives a more transparent understanding of the orbital ordering (symmetry equivalent to quadupolar ordering[15]; See Appendix A).The $j=3/2$-$1/2$ mixing will also allow to us to understand the T-dependent effective moment and the unusual high temperature susceptibility.

We analyze $H_{\rm eff}$ using a four-site mean field theory (MFT); see Fig. 1(a). At each site i there are 15 mean fields $\langle\boldsymbol{S}_i\rangle$, $\langle n_i^\alpha\rangle$ and $\langle\boldsymbol{S}_i n_i^\alpha\rangle$, and 4 constraints $\sum_\alpha\langle n_i^\alpha\rangle=1$ and $\sum_\alpha\langle\boldsymbol{S}_i n_i^\alpha\rangle=\langle\boldsymbol{S}_i\rangle$. We solve for $4\times(15-4)=44$ variables to find the lowest energy solution of the MFT equations; see Appendix B.

Orbital Ordering: At high temperatures $n^{yz} = n^{zx} = n^{xy} = 1/3$. There is an onset of orbital ordering, with preferential orbital occupancy (see Figure 1(d)), at temperature T_o determined by both V and $J_{\rm SE}$. Moreover, we find that V and $J_{\rm SE}$, individually and together, lead to the same orbital ordering pattern. Magnetic order develops at a T_c determined by $J_{\rm SE}$, with $T_c < T_o$ independent of parameters[26]; see Appendix D.

Figure 1(b) shows the orbital ordering pattern. On each site we only show the two orbitals with significant occupancy, with the lowest occupancy orbital omitted. For the two sites in the lower plane, these are the yz and xy orbitals; while for the two sites in the upper plane the roles of yz and zx orbitals are reversed.

We now discuss how orbital ordering explains the puzzles highlighted in the Introduction.

(a) Entropy: L and S add up to $j = 3/2$ with a high temperature entropy of $R \ln 4$. Below T_o, orbital ordering splits the $j = 3/2$ quartet into two Kramers doublets, leading to an $R \ln 2$ entropy. The remaining spin entropy is released at T_c, consistent with experiments[8,9].

(b) Local Moments: Naively, the local magnetic moment vanishes in d^1 systems. The t_{2g} orbital has effective $L=-1$ and $S=1/2$ leading to $\boldsymbol{M} = 2\boldsymbol{S} - \boldsymbol{L} = 0$. Equivalently, the projection of $\boldsymbol{M}$ to the $j = 3/2$ subspace is zero. The observed non-zero moment arises from a combination of the reduction[13,14] of the orbital moment due to (a) covalency with oxygen; (b) dynamical Jahn-Teller effects, and (c) orbital ordering. As we show here, (c) also explains the strong T-dependence of the local moment not easily understood in terms of (a) and (b).

Note that full orbital polarization ($n_i^\alpha = 1$ for some α and zero for others) is time-reversal invariant and does not generate an $\boldsymbol{L}$. However, SOC creates a superposition of orbitals instead of the occupancy being concentrated in a single orbital. The resulting partial occupancy of at least two orbitals as in Fig. 1(d) then allows for the development of $\boldsymbol{L}$, pointing along the intersection of the two occupied planes with direction (e.g., $\pm x$) selected by the spin interactions characterized both by J_H/U and the magnitude of the orbital order parameter.

One of our key results is that orbital order results in $j = 3/2$-$1/2$ the mixing, leading to a T-dependent moment, even in the absence of covalency with oxygen, which has not been recognized so far. To understand this general result, it is useful to look at the limit $J_{SE} = 0$, with $T_c=0$ and orbital order driven by V, where we can find analytical results; see Appendix E. We find that the orbital ordering shown in Fig. 1(b) leads to a local moment $\mu_{\rm eff}(T) = 172V|\delta n_x(T)|\mu_B/9\lambda$. The orbital order parameter $\delta n_x(T) = \langle n^{yz}\rangle - \frac{1}{3}$ (for the most occupied orbital) leads to the T-dependence of $\mu_{\rm eff}(T)$.

(c) Magnetic Susceptibility: We find that orbital order impacts the susceptibility $\chi(T)$ in two ways. First, the reduced symmetry leads to an anisotropic response, so that χ is enhanced in the ordering planes but reduced in the perpendicular direction. Second, $\chi(T)$ deviates from CW behavior due to the T-dependence of the effective moment $\mu_{\rm eff}$, and has a negative Θ as shown in Fig. 2.

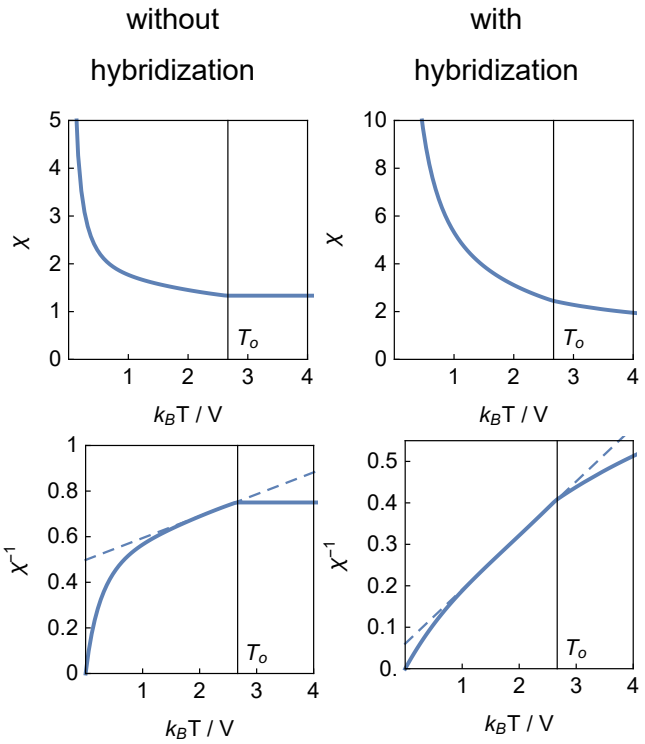

FIG. 2. Temperature dependence of the susceptibility, $\chi = \frac{1}{3}(\chi_{xx} + \chi_{yy} + \chi_{zz})$, and $1/\chi(T)$. Hybridization with surrounding oxygen atoms modifies the g-factor $\boldsymbol{M} = 2\boldsymbol{S} - \gamma\boldsymbol{L}$. Left panels: No hybridization ($\gamma = 1$), so there are no local moments above T_o and moments are formed only as a result of orbital order (see text). Right panels: with hybridization $\gamma = 0.536$. We have chosen $J_{\rm SE} = 0$ (so that $T_c = 0$) to illustrate the impact of orbital order below T_o on $\chi(T)$. Note that while a single Curie-Weiss (CW) fit cannot span the entire range below T_o, the the intercept from high temperatures has a negative intercept.

Magnetic Order: Orbital ordering impacts the exchange interactions in (4) and leads to the $T=0$ phase diagram in Fig. 1(c) with a canted FM state over much of the parameter regime, but a 4-sublattice AFM state favored in a small regime in $(J_{\rm SE}/\lambda, V/\lambda)$. We emphasize that while the Goodenough-Kanamori-Anderson rules[27–29] help us understand the sign of superexchange in Eq. (4) in terms of orbital occupancy, they are *not* sufficient to determine the long-range order. We see that the same underlying orbital order can give rise to either FM or AFM ground states due to interplay between various parameters.

From Fig. 1(b) we see that an electron in the highest occupancy yz (red) orbital in the lower plane, can hop into an essentially empty yz (red) orbital in the plane just above or below. This occupied-empty superexchange leads to a FM interaction in Eq. (4), resulting in a canted FM ground state, with a net ordered moment, in which the spins are FM aligned within each plane, but rotated by 90° from one plane to another as dictated by the or-

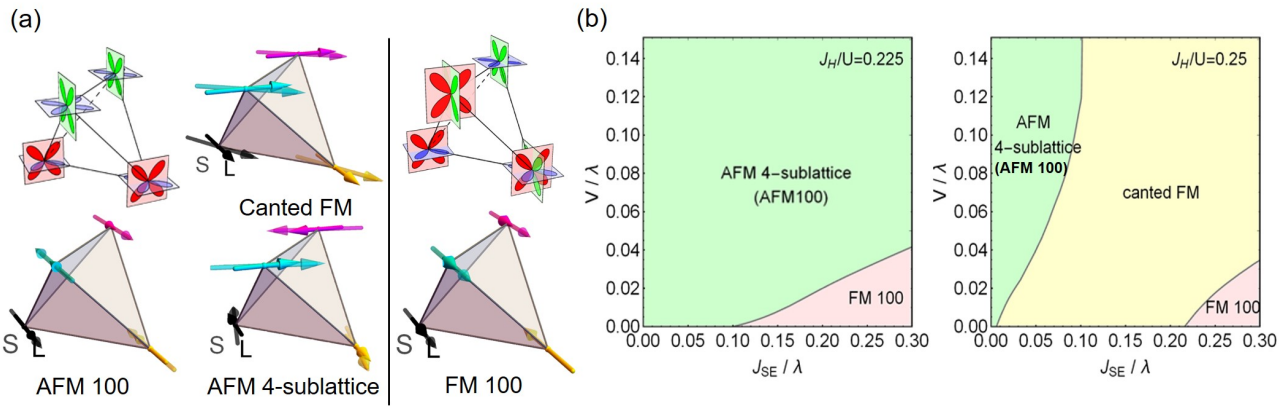

FIG. 3. Orbital ordering and magnetic order for $5d^2$ materials. (a) The canted FM, 4-sublattice AFM and AFM 100 phases share the same orbital order as in $5d^1$ systems in Fig. 1, while the FM 100 phase has a different orbital order. In general, the largest (smaller) occupancy orbitals are shown in solid (lighter) colors, and the smallest occupancy orbital is not shown. The lower right (yellow) site in the FM 100 state is an exception, where the red orbital almost fully occupied and two other two about half occupied. (b) $T=0$ phase diagrams for $J_H/U = 0.225$ and 0.25. In regimes where the 4-sublattice AFM is lowest in energy, we find that the AFM 100 state is essentially degenerate with it. Increasing J_H stabilizes the canted FM state.

bital ordering; see inset in Fig. 1(c). The 4-sublattice AFM structure (Fig. 1(c)) is stabilized over a larger parameter regime for weaker J_H/U (see Appendix G). Here the spins are AFM aligned in each plane, but again rotated by 90° from one plane to another.

d^2 Systems: In contrast to d^1 systems, d^2 materials are mostly AFM. We derive the microscopic d^2 Hamiltonian to understand why adding one extra t_{2g} electron, produces a sharp change in magnetism. The ground state of the Coulomb interaction (Eq. 2) for two electrons has $\mathbf{L}=1, \mathbf{S}=1$, which splits into $\mathbf{J}=0,1,2$ multiplets, with $\mathbf{J}=2$ the lowest in the presence of SOC. We might expect to recover $R\ln 5$ entropy across the magnetic transition, however, only $3.7\,J/(\mathrm{mol}\,K) < R\ln 2 = 5.76\,J/(\mathrm{mol}\,K)$ is recovered for Ba_2LuReO_6[30]. The missing entropy hints once again at a hidden order, which preserves time reversal, above the magnetic transition.

For d^2 system, the hopping, on-site Coulomb and inter-site electric-quadrupole interactions have the same form as in the d^1 case, but the SOC and the superexchange are modified. The SOC projected to the $\mathbf{L}_i = 1, \mathbf{S}_i = 1$ ground state manifold for d^2 system is $H_{\rm SO} = -\lambda/2 \sum_i \mathbf{L}_i \cdot \mathbf{S}_i$. We can derive the superexchange Hamiltonian for d^2 system

$$H_{\rm SE} = -\frac{J_{\rm SE}}{12} \sum_{\alpha} \sum_{\langle ij\rangle \in \alpha} \{ r_1 (2 + \boldsymbol{S}_i \cdot \boldsymbol{S}_j)(n_i^\alpha - n_j^\alpha)^2 + (1 - \boldsymbol{S}_i \cdot \boldsymbol{S}_j) \left[(n_i^\alpha + n_j^\alpha)^2 + (\tfrac{3}{2} r_3 - \tfrac{5}{2}) n_i^\alpha n_j^\alpha \right] \} \quad (5)$$

where the orbital occupancy n_i^α is defined in the two-electron basis, and $J_{\rm SE}$, r_1, r_3 are defined below Eq. (4).

A mean field analysis of $H_{\rm eff} = H_{\rm SO} + H_{\rm V} + H_{\rm SE}$ for d^2 systems leads to the orbital order and magnetic phases shown in Fig. 3. A major difference from d^1 is the dominance of AFM ordering in the d^2 case stabilized by the occupied-to-occupied AFM superexchange (unless J_H is made very large). See Appendix I for details on the magnetic phases and $\chi(T)$ of d^2 systems.

Relation to prior work: Our d^1 SE Hamiltonian in Eq. (4) differs in small ways from that of ref. 15, but is identical to that of ref. 19 (which focuses on 4d systems and ignores electric quadrupole interactions). Our d^2 SE Hamiltonian (5) is completely different from ref. 16. Also, our 4-site MFT has greater variational freedom than the 2-site MFT of ref. 15. Further, refs. 15,16 project down to the $j=3/2$ subspace (infinite λ limit), while we retain the mixing with $j=1/2$ that leads to our T-dependent effective moment. The orbital order that we describe is, however, symmetry equivalent to the quadrupolar order of refs. 15,16. See Appendix A for a detailed discussion.

Discussion: Recent experiments[31,32] on Ba_2MgReO_6 give x-ray evidence for small distortions consistent with our predicted orbital order; see Appendix H. Their magnetic order is also consistent with our canted FM [moments aligned in each plane but rotated between two planes (see Figure 1)], though their nomenclature[31,32] ([001] canted AFM) is different. The significant separation between T_o (33K for both Mg and Zn materials) and T_c (18K for Mg and 11K for Zn)[31,32] is consistent with the need to include V in the analysis. NMR[33] found a broken local point group symmetry in Ba_2NaOsO_6 above $T_c = 7$ K that persists up to 15 K, which could suggest $T_o \simeq 15$ K. However, this seems inconsistent with the loss of entropy[8,9] persisting up to much higher temperatures. Going forward, it would be useful to measure orbital ordering in d^1 and d^2 cubic double perovskites using techniques such as resonant X-ray scattering[34].

Acknowledgements We thank P.M. Woodward, J. Xiong, P. Tran, A. Paramekanti and R. Arita for useful discussions. We acknowledge support from NSF Materials Research Science and Engineering Center (MRSEC) Grants DMR-1420451 and DMR-2011876.

Appendix A: Comparison With Earlier Theoretical Works

Our work builds on the pioneering papers of Chen, Periera and Balents [15] on d^1 double perovskites, and Chen and Balents [16] on d^2 materials. Before going into details, we begin this appendix by summarizing the ways in which our paper differs from – and improves upon – refs. 15 and 16.

(a) The Hamiltonians differ in detail as described below. The differences are more significant for the d^2 case than d^1.
(b) Our mean field analysis uses four inequivalent sites per unit cell, as opposed to two sites in the earlier papers, and thus has greater variational freedom. (a) and (b) account for the differences in the phase diagrams.
(c) We use the (L, S)-basis while they use of the J basis, which allows us to retain the mixing of $J = 3/2$ with $J = 1/2$ (ignored in earlier papers) and leads to the T-dependent effective moments in the orbitally ordered state.
(d) Our orbital ordering is equivalent to the quadropolar ordering of ref. 15 as discussed below.
(e) Finally, our focus is somewhat different from previous works. In addition to the ground state magnetic phase diagram, we focus on finite temperature properties such as the loss of entropy and the non-Curie-Weiss form of the susceptibility, both of which we attribute to orbital ordering.

Hamiltonians: For the d^1 case, the superexchange Hamiltonian H_{SE} in eq. (4) of our paper is similar to eqs. (13) and (18) of ref. [15] however, there are small differences. Ref. [15] treats the AFM and FM couplings as independent parameters, while the superexchange scale $J_{\rm SE}$ and Hund's coupling J_H/U determine our AFM and FM couplings. From this perspective, we may say that our eq. (4) includes a term missing in ref. [15]. Rewriting the second line in eq. (4) as $+J_{SE}(\boldsymbol{S}_i\boldsymbol{S}_j - 1/4)[r_2/4(n_i^\alpha - n_j^\alpha)^2 + (2r_2 + r_3)/3(n_i^\alpha n_j^\alpha)]$ we can see that the $r_2/4(n_i^\alpha - n_j^\alpha)^2$ piece is effectively absent in ref. [15].

The difference in the d^2 case is more severe. The d^2 Hamiltonian used in ref. [16] had the same form as the d^1 Hamiltonian of ref. [15], except for replacing the spin and orbital operators by operators appropriate for the d^2 case. This differs from our superexchange Hamiltonian in eq. (5), which we derived using a strong coupling expansion for the d^2 case. It is evident that our d^2 Hamiltonian in eq. (5) does *not* have the same form as our d^1 Hamiltonian in eq. (4).

A recent work [19], focused on the spin-dimer phase in $4d^1$ materials. They used the same d^1 superexchange Hamiltonian as our eq. (4), however they did not take into account the electric quadrupole-quadrupole interaction term of eq. (3), which may be justified for $4d$ materials since the spatial extent of the orbitals is smaller than in the $5d$ case of interest that we focus on. We also note that the dimer phase found in ref. [19] is stabilized for parameter values (small $\eta = J_H/U$ and intermediate SOC) relevant for the $4d^1$ materials.

2 site vs 4 site mean field theory: Ref. [15] considered a two-site ansatz in their d^1 mean field theory (MFT), while we analyze a more general MFT that allows for four inequivalent sites, which impacts phase diagram. For instance, using a four-site MFT enables us to find an AFM 4-sub lattice ground state, as compared to AFM 100 phase in ref. [15] (which is not a stable solution in our MFT). Our canted FM ground state is similar to the FM 110 phase in [15]; both are in fact two sublattice structures. Details of the MFT are described in Appendix B.

$J = 3/2, 1/2$ mixing: We choose to work in the full $t_{2g} \otimes \sigma$ basis or $L \otimes S$ basis, which is equivalent to working in the J-basis used in refs. [15,16]. The equivalence is detailed below for convenience, and this also shows the equivalence between orbital ordering in the LS basis and quadrupolar ordering in the J basis.

The key difference difference is that the authors of refs. [15,16] project into the total angular momentum $J = 3/2$ states, effectively taking the SOC $\lambda \to \infty$, while we do not take this limit. It is important to ask *why* we need to retain the mixing between the $J = 3/2$ and $1/2$ states, separated by an energy of $3\lambda/2$, or equivalently keep keep the full $t_{2g} \otimes \sigma$ manifold, for $5d$ materials where SOC is large? As shown in the main text, and elaborated on here this mixing is responsible for the effectively T-dependent magnetic moment below the orbital ordering temperature, and the resulting non-Curie Weiss form of the magnetic susceptibility.

As already noted in the main paper, there is no magnetic moment for transition metal ion with one electron in the t_{2g} sector $\boldsymbol{M} = 2\boldsymbol{S} - \boldsymbol{L} = 0$, in the limit where we ignore the hybridization of the TM d-orbitals with the p orbitals of neighboring oxygen ligands. Including the later effect (see, e.g., eqs. (8-12) in ref. [15]) leads to a small non-zero magnetic moment, but cannot explain the observed non-Curie Weiss behavior of the susceptibility $\chi(T)$ above the magnetic ordering temperature.

Our analysis, explains this behavior of $\chi(T)$ by relating the effective local moment to the T-dependent orbital occupancy below the orbital ordering temperature. As detailed in Appendix E, this involves the mixing between the low-energy $J = 3/2$ manifold (L parallel to S) and $J = 1/2$ subspace (L anti-parallel to S). Physically, this mixing leads to a small misalignment between the spin and orbital angular momenta, which contributes to a non-zero magnetic moment (see Fig. 1). This reveals how T-dependent non-zero magnetic moments can arise, even in the limit where we ignore the hybridization-led (T-independent) contribution to the moment. In the main text, we show in Fig. 2 the susceptibilities including both the contribution of the T-dependent moments arising from orbital order and that of the hybridization with oxygen.

LS and J-basis operators: Here we summarize, for convenience, the relationship between the spin and or-

bital occupancy operators that we use, and the dipole **J**, quadrupole **O** and octupole **T** operators used in refs. [15,16].

The transformation process involves two steps: (i) a unitary transformation from the $L \otimes S$ basis to the total angular momentum J basis, and (ii) projecting out the high energy $J = 1/2$ suspace, and focusing on the $J = 3/2$ manifold. We find

$$\vec{S} \to \frac{1}{3}\vec{J}, \quad \vec{L} \to \frac{2}{3}\vec{J}. \tag{A.1}$$

To write down the orbital occupancies in terms of the J_i's, we need to define quadrupole operators

$$\begin{aligned} O_{3z^2-r^2} &= J_z^2 - \frac{1}{2}(J_x^2 + J_y^2) \\ O_{x^2-y^2} &= \frac{\sqrt{3}}{2}(J_x^2 - J_y^2) \end{aligned} \tag{A.2}$$

Using these definitions, one can write

$$\begin{aligned} n^{yz/zx} &\to \frac{1}{3} + \frac{1}{9}O_{z^2} \mp \frac{1}{3\sqrt{3}}O_{x^2-y^2} \\ n^{xy} &\to \frac{1}{3} - \frac{2}{9}O_{z^2} \end{aligned} \tag{A.3}$$

From here we see clearly that the orbital order that we discuss in the main text is equivalent to "quadrupolar order", which does not break time-reversal invariance.

Finally, to write the operators $S^a n^\alpha$, we need to define the octupole operators

$$\begin{aligned} T_x^\alpha &= J_x^3 - \frac{1}{2}(\overline{J_x J_y^2} + \overline{J_z^2 J_x}) \\ T_x^\beta &= \frac{\sqrt{15}}{6}(\overline{J_x J_y^2} - \overline{J_z^2 J_x}) \end{aligned} \tag{A.4}$$

where we use the over-bar to denote symmetrization of the operators: $\overline{AB^2} = ABB + BAB + BBA$. We can then write

$$\begin{aligned} S^x n^{yz} &\to \frac{1}{15}J_x - \frac{2}{15}T_x^\alpha \\ S^x n^{zx} &\to \frac{2}{15}J_x + \frac{1}{15}T_x^\alpha - \frac{1}{3\sqrt{15}}T_x^\beta \\ S^x n^{xy} &\to \frac{2}{15}J_x + \frac{1}{15}T_x^\alpha + \frac{1}{3\sqrt{15}}T_x^\beta \end{aligned} \tag{A.5}$$

Appendix B: Mean Field Theory

We solve the low-energy Hamiltonian $H_{\text{eff}} = H_{SE} + H_V + H_{SO}$ (defined in the main text) within mean field theory. We choose a conventional unit cell of the FCC lattice with 4 transition metal (TM) ion sites, each with 12 nearest neighbors (NN). The inter-site interactions separate into three inequivalent groups depending on whether the NN sites lie on yz, zx or xy planes. These terms are factorized as $\hat{\mathcal{O}}_i\hat{\mathcal{O}}_j \approx \langle\hat{\mathcal{O}}_i\rangle\hat{\mathcal{O}}_j + \hat{\mathcal{O}}_i\langle\hat{\mathcal{O}}_j\rangle - \langle\hat{\mathcal{O}}_i\rangle\langle\hat{\mathcal{O}}_j\rangle$, where the expectation values $\langle\mathcal{O}_i\rangle$ are the "mean fields". Specifically, we factorize the superexchange H_{SE} and quadrupole interactions H_V using

$$\begin{aligned} S_i^a S_j^a n_i^\alpha n_j^\alpha &\approx S_i^a n_i^\alpha \langle S_j^a n_j^\alpha\rangle + \langle S_i^a n_i^\alpha\rangle S_j^a n_j^\alpha \\ &\quad - \langle S_i^a n_i^\alpha\rangle\langle S_j^a n_j^\alpha\rangle \\ S_i^a S_j^a n_i^\alpha &\approx S_i^a n_i^\alpha \langle S_j^a\rangle + \langle S_i^a n_i^\alpha\rangle S_j^a - \langle S_i^a n_i^\alpha\rangle\langle S_j^a\rangle \\ n_i^\alpha n_j^\beta &\approx n_i^\alpha\langle n_j^\beta\rangle + \langle n_i^\alpha\rangle n_j^\beta - \langle n_i^\alpha\rangle\langle n_j^\beta\rangle \end{aligned} \tag{B.1}$$

The spin-orbit interaction H_{SO} contains only on-site terms and does not need mean field decomposition.

At each site, we have a total of 15 mean fields: 3 $\langle S_i^a\rangle$ ($a = x, y, z$), 3 $\langle n_i^\alpha\rangle$ ($\alpha = xy, yz, zx$) and 9 $\langle S_i^a n_i^\alpha\rangle$. There are four constraints at each site $\sum_\alpha n_i^\alpha = 1$ (for the d^1 case and 2 for d^1) and $\sum_\alpha S_i^a n_i^\alpha = S_i^a$. Hence there are $(15 - 4) = 11$ *independent* variables at each site and a total of $(11 \times 4) = 44$ "mean fields" in our 4-site unit cell.

The resulting mean-field Hamiltonian is a sum of single-site terms which depend on the mean fields $\langle\mathcal{O}_i\rangle$ that need to be determined self-consistently. We use an iterative, numerical procedure to solve this problem self-consistently. Starting with an initial guess for the (input) mean fields, we solve for the the eigenvalues and eigenvectors of the single site Hamiltonian, using which we compute the expectation values that define the (output) mean fields. The procedure is iterated until the input and output mean fields converge. To improve the rate of convergence, we find it useful to mix the output values with some fraction of the inputs from the previous iteration. We ground state magnetic phase diagram is determined by finding the lowest energy solution for each set of couplings J_H, J_{SE}, V, λ.

Appendix C: Parameter Estimates

The parameters of the multi-orbital Hamiltonian for double perovskites are: hopping t between orbitals on nearest neighbor sites, the on-site Coulomb repulsion U, the spin-orbit coupling λ, the Hund's coupling J_H and the nearest neighbor electric quadrupole-quadrupole interaction V.

Ref. [9] estimates the hopping parameter $t \approx 50 - 100$meV based on the overlap integral between two sites and $U = 3.3$eV from the Coulomb integrals of the effective charge distribution on a site. Further, Ref. [10] obtains the electronic structure using DFT (within the GGA approximation and including SOC and U) and provide an estimate for the t_{2g} bandwidth $W \approx$ 1eV and $U \approx 3$eV. Since the bandwidth $W = 2zt$, where $z = 12$ is the number of the neighbors, we obtain the estimate $t \approx 42$meV which is consistent with Ref. [9]. In our calculations we use $t \approx 50$meV and $U = 3$eV and using these values we estimate the superexchange energy scale $J_{SE} = 4t^2/U \approx 3.3$meV.

The analysis in Refs. [24,35] based on RPA, estimates the Hund's coupling to be $J_H \approx 0.5$eV. More recently, the values of J_H and spin orbit coupling λ have been deduced from resonant inelastic x-ray scattering[22,23]. J_H depends on the d-count and the row transition metal ion is in. For $5d$ transition metal compounds, $J_H \approx 0.23 - 0.275$eV and $\lambda \approx 0.34 - 0.425$eV.

Finally we turn to V, the strength of the electric quadrupole-quadrupole interaction, which is the least known of the parameters entering our Hamiltononian. R. Arita (private communication) has estimated it to be 10 meV from DFT which is comparable to superexchange. We give here a very crude estimate that gives some physical insight, but given the uncertainty in its value we discuss in Appendix D the extent to which our results depend on the value of V relative to the superexchange.

The t_{2g} orbitals carry quadrupole moments and their inter–site repulsion can be large because of the large spatial extent of the 5d orbitals[15]. The traceless electric quadrupole tensors for xy, yz, zx orbitals (superscripts) in the Cartesian basis with subscripts i and j taking values $\{x, y, z\}$ are given by:

$$Q_{ij}^{(xy)} = \begin{bmatrix} Q & 0 & 0 \\ 0 & Q & 0 \\ 0 & 0 & -2Q \end{bmatrix},$$
$$Q_{ij}^{(yz)} = \begin{bmatrix} -2Q & 0 & 0 \\ 0 & Q & 0 \\ 0 & 0 & Q \end{bmatrix}, \qquad \text{(C.1)}$$
$$Q_{ij}^{(zx)} = \begin{bmatrix} Q & 0 & 0 \\ 0 & -2Q & 0 \\ 0 & 0 & Q \end{bmatrix},$$

The magnitude of the quadrupole moment

$$\begin{aligned} Q &= \int |\psi^{(xy)}(\vec{r})|^2 (3x^2 - r^2) d^3\vec{r} \\ &= \int |\psi^{(xy)}(\vec{r})|^2 (3y^2 - r^2) d^3\vec{r} \\ &= -\tfrac{1}{2} \int |\psi^{(xy)}(\vec{r})|^2 (3z^2 - r^2) d^3\vec{r} \qquad \text{(C.2)} \end{aligned}$$

is obtained from the charge distribution of the $5d$ ionic wave function.

To estimate the electric quadrupole moment Q, we model the t_{2g} "ionic" wave function $\psi^{(xy)}(\vec{r})$ as the product of an "angular" wave function $Y_{xy} = \sqrt{60/16\pi}(xy/r^2)$ with the $n = 5, l = 2$ radial wave function in a Coulomb potential $-Z_{\rm eff}e^2/r$. We thus obtain $Q = \beta e a_0^2/Z_{\rm eff}^2$ with $\beta = 385.7$ and Bohr radius $a_0 = 5.3 \times 10^{-11}$m.

Next we find V using the electrostatic energy[15] $V = k_e 9\sqrt{2}Q^2/a^5$, where a is the lattice constant of the double perovskite FCC lattice. Note $a = \sqrt{2}\ell$, where ℓ is the distance between neighboring B' atoms. For the 5d $BaNaOsO_6$ compound $\ell = 5.8$Å. We use the dielectric constant $k_e = \frac{1}{4\pi\epsilon_0} = 14.4eV$Å$/e^2$; since this is "short distance physics" we do *not* use the macroscopic ϵ. Using quadrupole moment Q derived above we find that $V \simeq 60/Z_{\rm eff}^4$ eV.

An equivalent way to understand this estimate of the electric quadrupole interaction is to say that, on dimensional grounds, $Q = eR^2$ where the length scale $R = \gamma a_0$ with γ a dimensionless parameter of order unity. Again, using $V = k_e 9\sqrt{2}Q^2/a^5$, we find that $V \simeq 0.4\gamma^4 meV$. This shows that small errors in estimating the "size" of the orbital wave-function γ will lead to a large error in the estimate of V.

Appendix D: Orbital Ordering T_o And Spin Ordering T_c: Role Of V And $J_{\rm se}$

We saw in Appendix C that the electric quadrupole interaction energy scale V could well be comparable to the superexchange scale J_{se}. However, given the uncertainty in the estimation of V we would like to make sure about aspects of our results that are independent of the strength of V relative to J_{se}.

We show here that the orbital ordering T_o is always larger than the spin ordering T_c independent of V, though the separation between the two phase transitions does depend of V. In Fig. 4 we plot T_o and T_c as a function of J_{se} at a fixed $\eta = J_H/U = 0.2$. The left panel in the figure shows results for small $V = 0.001\lambda \simeq 0.4$ meV while the right panel for larger $V = 0.025\lambda \simeq 10$ meV (where we use $\lambda \sim 0.4eV$ for 5d transition metal ions). Our results show that both V and J_{se} act in concert to lead to the same orbital order while only J_{se} leads to magnetic order.

Referring back to the phase diagram in Fig. 1(c) we should also note that the very small $V = 0.001\lambda$ regime is "fine tuned" in so far as magnetism is concerned, with a 4-sublattice AFM state, while over most of the parameter regime the canted FM is stabilized.

Appendix E: Orbital Order, T_o And $\mu_{\rm eff}(T)$ For d^1 Model

.

Our goal in this appendix is to gain insight into the onset and nature of orbital ordering, and how it leads to a mixing between $j = 3/2$ and $1/2$ resulting in a T-dependent local moment. In order to make analytical progress on these questions, we analyze a special limit: we set the superexchange $J_{se} = 0$ in this appendix so that the magnetic T_c vanishes; this allows us to focus on orbital ordering.

We solve the mean field equations for $H_{\rm V} + H_{\rm SO}$ analytically. The relevant mean field parameters for the four sites from Fig. 1(b) are given by

$$\langle n_1^{xy} \rangle = \langle n_2^{xy} \rangle = \langle n_3^{xy} \rangle = \langle n_4^{xy} \rangle = \tfrac{1}{3} + \delta n_z \qquad \text{(E.1)}$$

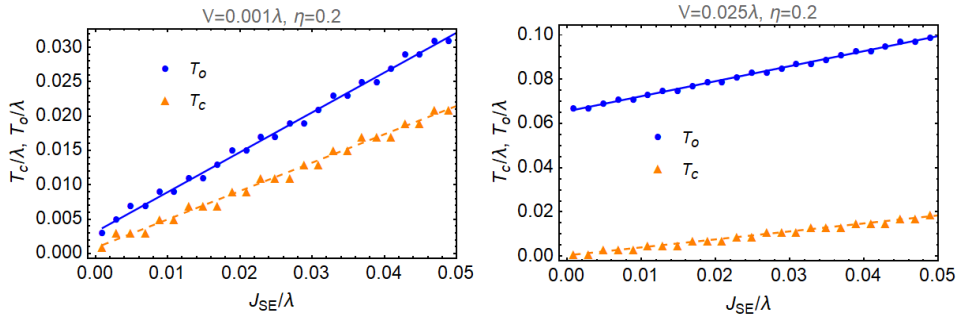

FIG. 4. T_c and T_o as a function J_se for small $V = 0.001\lambda$ (ground state is AFM 4-sublattice) and $V = 0.025\lambda$ (ground state is canted FM).

$$\langle n_1^{yz}\rangle = \langle n_2^{yz}\rangle = \langle n_3^{zx}\rangle = \langle n_4^{zx}\rangle = \tfrac{1}{3} + \delta n_x \tag{E.2}$$

with the condition $\sum_\alpha n_i^\alpha = 1$ determining the other four parameters. We obtain the single site mean field Hamiltonian for V.

$$H'_{\rm V} = -V\left[(\tfrac{86}{3}\delta n_x + \tfrac{43}{3}\delta n_z)n^{yz} + (\tfrac{43}{3}\delta n_x + \tfrac{53}{3}\delta n_z)n^{xy}\right] \tag{E.3}$$

In the absence of magnetism, the mean field Hamiltonian $H'_{\rm MF} = H'_{\rm V} + H_{\rm SO}$ is time reversal invariant, and we rotate into the basis of total angular momentum j which factors into two 3×3 blocks of doublets. The upper block may be chosen to be of the form

$$\begin{pmatrix} \frac{3\lambda}{2} & -\frac{43V(2\delta n_x+\delta n_z)}{3\sqrt{6}} & -\frac{7V\delta n_z}{\sqrt{2}} \\ -\frac{43V(2\delta n_x+\delta n_z)}{3\sqrt{6}} & \frac{7V\delta n_z}{2} & \frac{43V(2\delta n_x+\delta n_z)}{6\sqrt{3}} \\ -\frac{7V\delta n_z}{\sqrt{2}} & \frac{43V(2\delta n_x+\delta n_z)}{6\sqrt{3}} & -\frac{7V\delta n_z}{2} \end{pmatrix} \tag{E.4}$$

where the upper block basis $|j, m_j\rangle$ is given by $\{|1/2,+1/2\rangle,\ |3/2,-3/2\rangle,\ |3/2,+1/2\rangle\}$ (in this order). The lower block is the time reversal partner of the upper block.

We rotate the (upper block) Hamiltonian so that it is diagonalized in the $j = 3/2$ subspace $\{|3/2,-3/2\rangle, |3/2,+1/2\rangle\}$)

$$\begin{pmatrix} \frac{3\lambda}{2} & x & y \\ x & \Delta & 0 \\ y & 0 & -\Delta \end{pmatrix}. \tag{E.5}$$

Here

$$\Delta = V\frac{\sqrt{1849\delta n_x(\delta n_x+\delta n_z)+793\delta n_z^2}}{3\sqrt{3}} \tag{E.6}$$

and

$$x = -V\frac{43\sqrt{3}(2\delta n_x+\delta n_z)\cos\frac{\theta}{2} + 63\delta n_z \sin\frac{\theta}{2}}{9\sqrt{2}} \tag{E.7}$$

with $\theta = \arctan 43\sqrt{3}\,(2\delta n_x + \delta n_z)\,/63\delta n_z$. The expression for y is given by changing $\sin(\theta/2) \to \cos(\theta/2)$ and $\cos(\theta/2) \to -\sin(\theta/2)$ in x.

Next we derive the mean field equation for the orbital order parameter. In the large λ limit, δn_z is very small (see Appendix F and Fig. 2) at all T and we can simply set $\theta = \pi/2$. The orbital order parameter is the expectation value of the operator, $\delta n_x \to n^{yz} - \frac{1}{3}$, whose into the 2×2 subspace of energies $-\Delta$ and Δ is given by

$$\delta\hat{n}_x \to \begin{pmatrix} -\frac{1}{2\sqrt{3}} & -\frac{1}{6} \\ -\frac{1}{6} & \frac{1}{2\sqrt{3}} \end{pmatrix} \tag{E.8}$$

The self-consistent mean equation for δn_x is

$$\delta n_x = \langle\delta\hat{n}_x\rangle = \frac{1}{2\sqrt{3}}\tanh\beta\Delta \tag{E.9}$$

where $\Delta \approx \frac{43V}{3\sqrt{3}}\delta n_x$. The orbital ordering transition temperature T_o is the temperature below which Δ becomes nonzero. Linearizing the MF equation we get

$$k_B T_0 = 43V/18 \tag{E.10}$$

Next, we look at effective magnetic moment. We project the magnetization operator $\boldsymbol{M} = 2\boldsymbol{S} - \boldsymbol{L}$ onto the low-energy subspace. Nominally $g = 0$ for the $j = 3/2$ states, and the first non-zero correction to the wavefunction comes from mixing of the $j = 3/2$ and $j = 1/2$ states. This mixing is described by the lowest doublet with energy $-\Delta$:

$$\begin{pmatrix}\psi_{\rm u}\\ \psi_{\rm d}\end{pmatrix} = \begin{pmatrix} -\frac{2x}{3\lambda}\,|\frac{1}{2},+\frac{1}{2}\rangle + \cos\frac{\theta}{2}\,|\frac{3}{2},-\frac{3}{2}\rangle + \sin\frac{\theta}{2}\,|\frac{3}{2},+\frac{1}{2}\rangle \\ +\frac{2x}{3\lambda}\,|\frac{1}{2},-\frac{1}{2}\rangle + \cos\frac{\theta}{2}\,|\frac{3}{2},+\frac{3}{2}\rangle + \sin\frac{\theta}{2}\,|\frac{3}{2},-\frac{1}{2}\rangle \end{pmatrix}. \tag{E.11}$$

We start with the $\boldsymbol{M}$ operator in $|L_z S_z\rangle$ basis and apply the same set of transformations above as that in $H'_{\rm MF}$ to obtain $\boldsymbol{M}'$. Then the projected matrix elements of the magnetization operator can be extracted via $\langle\alpha|\,\boldsymbol{M}'\,|\alpha'\rangle$ with $\alpha,\alpha' \in \{\psi_{\rm u},\psi_{\rm d}\}$, keeping only terms of order $\frac{V}{\lambda}$. From the projection, we obtain the g factors for this doublet in all three directions (ie. $M_x = g_x\frac{\mu_B}{2}\sigma_x$, etc) and compute the average g factor obtained in a powder susceptibility measurement $g^2 = \frac{1}{3}\left(g_x^2 + g_y^2 + g_z^2\right)$ to obtain the powder average effective moment for the doublet. For simplicity, we continue to work in the approximation where $\delta n_z = 0$. The g factor is then given by

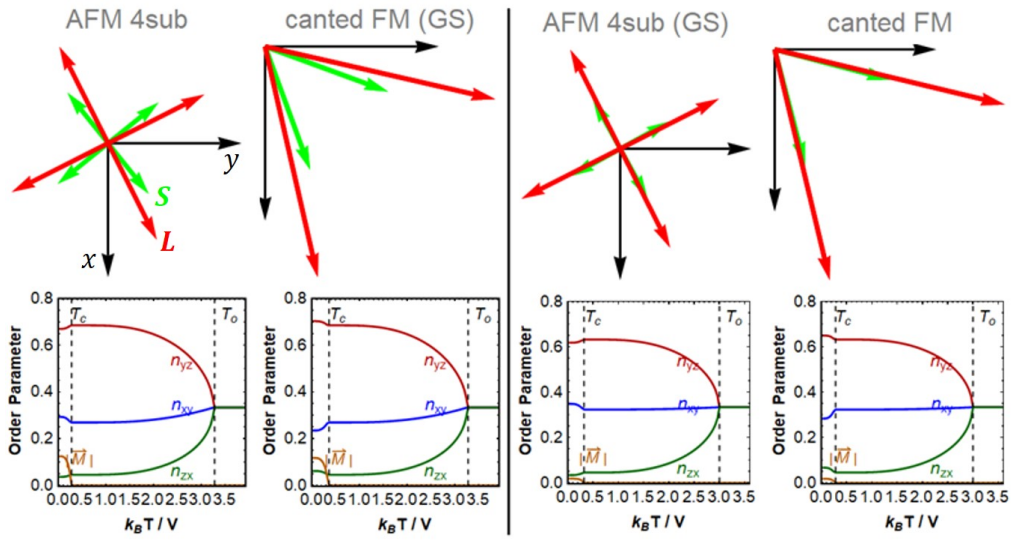

FIG. 5. Left panel: magnetic structures and order parameters at $J_{SE} = V = \lambda/40, J_H/U = 0.2$ (typical parameter values used in our paper). The ground state is found to be canted FM and L and S though correlated are not perfectly aligned. Right panel: magnetic structures and order parameters at $J_{SE} = V = \lambda/240, J_H/U = 0.2$ (to make contact with the very large lambda limit). The corresponding ground state is found to be the 4–sublattice AFM. L and S are almost perfectly aligned and $n_{xy} \approx 1/3$. The different magnetic ground states in the two cases can be understood in terms of phase diagram of Fig. 1(c) in the main paper.

$g = 344V|\delta n_x|/9\sqrt{3}\lambda$, so that the moment is

$$\mu_{\rm eff} = 172V|\delta n_x|\mu_B/9\lambda. \tag{E.12}$$

This shows how orbital order leads to the development of a T-dependent magnetic moment below T_o.

Appendix F: Comparison Of Finite λ And Very Large λ Results

In this appendix we compare the dependence of the orbital order parameters and magnetic structures on the SOC strength λ. (A) The left panels in Fig. 5 show the results for a "finite" λ with $J_{\rm SE} = V = \lambda/40$, which is the parameter set used in main text. (B) These are to be contrasted with the right panels in Fig. 5 where we have chosen λ with $J_{\rm SE} = V = \lambda/240$ to mimic the "infinite" λ limit (similar to Ref. 15).

We note three main differences between case (A) and (B) in Fig. 5. First, the orbital order parameters are simpler in the large λ limit with $n_{xy} = 1/3$, or in the notation of Appendix E $\delta n_z \equiv 0$ for all T. Second, the magnetic order stabilized in the ground state is different in the two cases as indicated in Fig. 5. This can be easily understood in terms of $T = 0$ phase diagram of Fig. 1(c) in the main paper, from which we see that the parameters in case (A) lead to a canted FM while that in case (B) to a AFM (4-sublattice) ground state. Third, the angle between $\mathbf{L}$ and $\mathbf{S}$ decreases with increasing SOC. At large λ, we have perfect alignment of $\mathbf{L}$ and $\mathbf{S}$, which leads to a vanishing $\mathbf{M} = 2\mathbf{S} - \mathbf{L}$ for $T_c < T < T_o$ (in the absence of hybridization with oxygen).

Using an approach similar to Appendix E , we can can solve for the mean field orbital ordering, which in the infinite SOClimit is exactly the same as the quadropolar ordering of Ref. 15. A mean field analysis of $H_V + H_{SE}$ projected into the $j = 3/2$ subspace (infinite SOC limit) leads to an orbital ordering temperature

$$T_o = \frac{43}{18}V + \frac{J_{SE}}{4}r_1 - \frac{J_{SE}}{18}(r_3 + r_2/2). \tag{F.1}$$

This essentially matches the result in Ref. 15, except for minor difference due to the missing piece of the AFM superexchange interaction discussed in Appendix A.

Appendix G: Phase Diagram With Varying J_H/U For $5d^1$ Systems

We next consider the dependence of the $T = 0$ magnetic phase diagram on Hund's coupling $\eta = J_H/U$. We show in Fig. 6 how phase diagram in the superexchange-electric quadrupole interaction plane $(J_{\rm SE}/\lambda, V/\lambda)$ evolves with Hund's coupling $\eta = J_H/U$. As expected, the canted FM phase dominates over the AFM phase with increasing η.

Appendix H: Orbital Ordering And Distortions

In this appendix, we give a qualitative discussion of how orbital ordering in $5d^1$ system distorts the oxygen octahedra and its averaged effect over a unit cell of the FCC lattice.

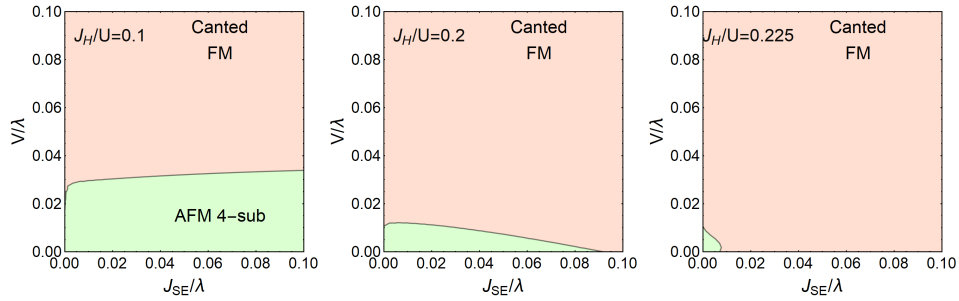

FIG. 6. Phase diagram as a function of the inter-site quadroplar repulsion V and the superexchange scale J_{SE} measured in units of the spin-orbit coupling scale λ for different values of the Hund's coupling (measured in units of the onsite Coulomb repulsion U) with J_H/U ranging from 0.1 to 0.225. As we increase $\eta = J_H/U$, the canted FM phase dominates over the AFM 4-sublattice phase for large $J_{\rm SE}/\lambda$. Phase diagram for $J_H > 0.25$ is filled with canted FM for almost all relevant parameters J_{SE} and V.

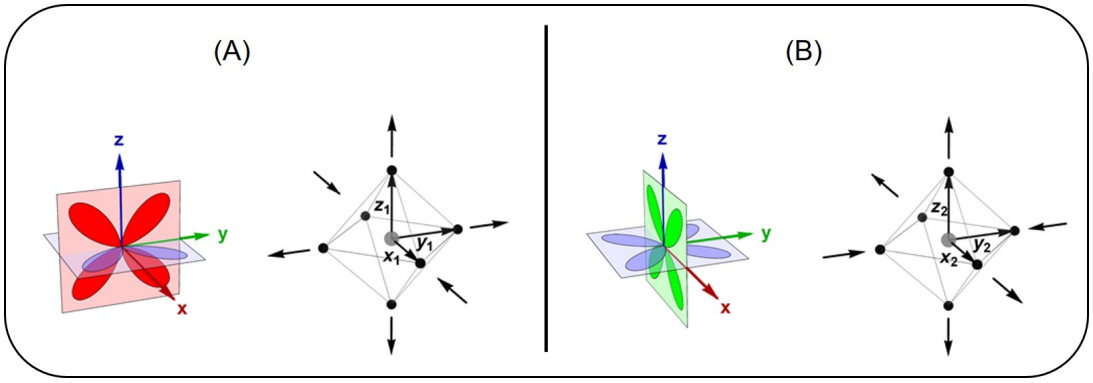

FIG. 7. Distortion of oxygenb octahdra due to the onset of orbital ordering.

Let us recall the orbital order for $5d^1$ materials stabilized by a combination of the electric quadrupole–quadrupole interaction V and the superexchange $J_{\rm SE}$. As shown in Fig. 1(b) of the main text, the orbital order has a two sublattice structure with $n^{(1)}_{yz} > n^{(1)}_{xy} > n^{(1)}_{zx}$ on sublattice (1) (on the lower plane) and $n^{(2)}_{zx} > n^{(2)}_{xy} > n^{(2)}_{yz}$ on sublattice (2) (on the upper plane) As discussed in Appendix F, the results in the large SOC limit are qualitatively similar to those at finite SOC, but lead to a simpler physical picture. Hence, we focus on the infinite SOC limit for the following discussion. From Fig. 5 in Appendix F we see that in this limit, the low-T orbital occupancies for sublattices 1 and 2 can be approximately written as

$$\begin{aligned} n^{(1)}_{yz} &= 0.67, n^{(1)}_{xy} = 0.33, n^{(1)}_{xz} = 0 \\ n^{(2)}_{xz} &= 0.67, n^{(2)}_{xy} = 0.33, n^{(2)}_{yz} = 0 \end{aligned} \qquad \text{(H.1)}$$

Next let us look at the effect of orbital order on the oxygen cage that surrounds a transition metal (TM) ion by considering the Coulomb repulsion between electrons on the ligand and the TM. Let the undistorted distance between nearest O atom and the TM ion be d. Let $\pm x_i$ be the locations of the two O atoms located along the x–axis about the site i, and similarly $\pm y_i$ for O atoms located along y, and $\pm z_1$ for O atoms located along z axis. Then we expect (see Fig. 7) that

$$\begin{aligned} &y_1 - d > 0 \quad (\text{since } n^{(1)}_{yz} + n^{(1)}_{xy} = 1 > 0.67, \text{ the value in} \\ &\qquad\qquad \text{the high T phase with no orbital order}) \\ &z_1 - d = 0 \quad (\text{since } n^{(1)}_{yz} + n^{(1)}_{xz} = 0.67) \\ &x_1 - d < 0 \quad (\text{since } n^{(1)}_{xy} + n^{(1)}_{xz} = 0.33 < 0.67) \end{aligned} \qquad \text{(H.2)}$$

A positive (negative) sign means that the O atoms move away from (towards) the TM ion. This analysis is oversimplified. $z_1 - d$ is not strictly correct because the distribution of charges in the orbital ordered state and the high T state are not exactly the same, but $z_1 - d$ will certainly be much smaller in magnitude than the other displacements. The same argument around site 2 leads to $y_2 - d = x_1 - d < 0, z_2 - d = 0$, and $x_2 - d = y_1 - d > 0$. Since there an equal number of TM1 and TM2 sites in the unit cell, the average distortion along the x-direction is small, with $x_1 - d < 0$ and $x_2 - d > 0$ compensating each other, and the same for the distortion along the y-direction. In summary, while symmetry dictates that system will be tetragonal, the above argument shows qualitatively why the magnitudes of the distortion may be very small.

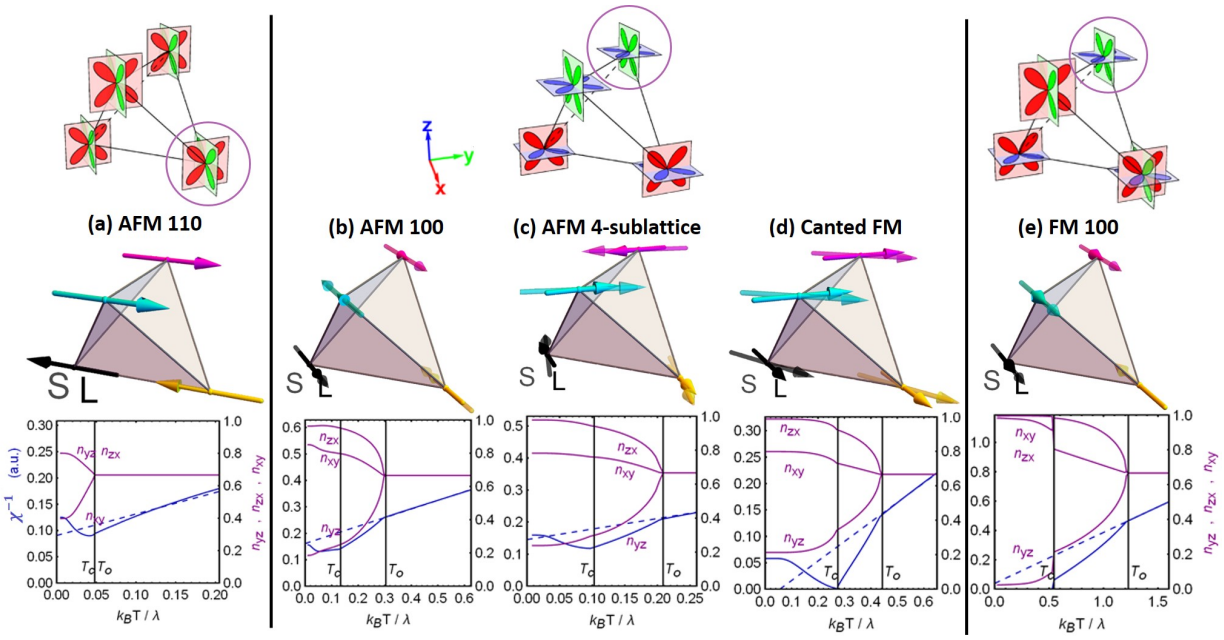

FIG. 8. Characteristic inverse susceptibility (blue) and orbital occupation (purple) curves are plotted against temperature for the three phases in Fig. 3: (a) AFM [110], (b) AFM [100], (c) AFM 4-sublattice, (d) canted FM and (e) FM [100]. Susceptibility is averaged over all three directions before being taken inverse of, $\chi^{-1} = 3(\chi_{xx} + \chi_{yy} + \chi_{zz})^{-1}$, and all sites in the tetrahedra. Dashed blue lines are high temperature linear fit of the inverse susceptibility for extracting the Curie constant: for all AFM phases, the Curie constants are negative; curie constant for canted FM is found to be positive whereas that of FM 100 phase is found to be very close to zero. Orbital occupancies are shown for the site circled in each plot.

Appendix I: Magnetic Susceptibility $\chi(T)$ For $5d^2$ Systems

Figure 8 shows the orbital occupations and inverse magnetic susceptibility as a function of temperature for the ground state phases obtained in the phase diagram (see main Fig. 3 (a)). At high temperature, the orbitals have uniform occupancy of $n^{yz} = n^{zx} = n^{xy} = 2/3$. At the orbital ordering temperature T_o, the orbitals begin developing unequal occupancies which grows with decreasing temperature. In this regime time-reversal symmetry is not broken. This is followed by a second transition at the magnetic ordering temperature T_c where time reversal symmetry is broken. We next discuss the behavior in the three AFM phases and the two FM phases below.

AFM [110] phase [Fig. 8(a)]: The two ordering temperatures T_o and T_c coincide and the electrons are pushed into the n_{yz} and n_{xz} orbitals to maximize antiferromagnetic superexchange. This orbital ordering by itself would not be favorable as the orbital repulsion is maximal in such a configuration. However, the transition is entirely driven by antiferromagnetic superexchange which then forces the orbital ordering shown, which also explain why $T_o \approx T_c$. Due to the strong orbital repulsion, this magnetic structure is favored only at small V. Note the contrast with the orbital ordering in d^1 systems (shown in the main paper Fig. 1 (b)) where the orbital repulsion is minimized and in this case its the orbital ordering that drives the magnetic structure. The high T Curie-Weiss magnetic susceptibility is fit with a negative Curie-Weiss constant θ_{CW}, as expected. We note that the orbital ordering for AFM110 is compatible with the tetragonal distortion seen in Sr_2MgOsO_6[6].

AFM [100], AFM 4-sublattice, Canted FM phases [Fig. 8(b-d)]: Next, we discuss three magnetic structures (AFM [100], AFM 4-sublattice, canted FM as shown in the main paper Fig. 3 (a) middle block) that share the same orbital ordering, which minimizes the inter-site orbital repulsion in the presence of spin orbital coupling. It is interesting to note that while the size of the moments are different, the magnetic ordering directions in the AFM 4-sublattice and canted FM phases for d^2 are the same as those in d^1 systems.

The AFM [100] is a new magnetic structure that arises only in d^2 systems. Even though it shares the same orbital ordering pattern as the AFM 4-sublattice and the canted FM, the orbital angular momenta of the two sites on the upper xy plane are suppressed compared to the two sites on the lower xy plane due to the different orbital occupancy on those planes. This happens because the orbital angular momenta are forced to lie along the [100] direction. We find that while the AFM [100] is not the ground state in our model, the energy difference with AFM 4-sublattice (AFM 4-sublattice becomes ground state in certain parameter regimes) is negligible, indicating that AFM [100] could be a competitive ground state in real materials.

For all the three magnetic structures, orbital ordering happens at a higher temperature than that of the magnetic phase transition. And yet the evolution of orbital occupations for the three magnetic structures exhibits differences: canted FM orbital occupations change rather more rapidly than those in the AFM phases. In addition, there is a secondary feature observed at a temperature $T' < T_c$ in the orbital occupancies, which shows a sudden change in behavior, and in the inverse susceptibility, which shows a tiny cusp, indicating effects of frustration between orbital and spin degrees of freedom.

For both AFM [100] and AFM 4-sublattice phases in Fig. 8(b),(c), $\chi(T)$ follows the Curie-Weiss law with a negative Curie-Weiss constant above T_o. Below T_o the orbital occupancies are temperature-dependent and the inverse susceptibility deviates from its high temperature behavior. Just below T_o, $\chi(T)$ can be fit to the Curie-Weiss law with a different negative Curie-Weiss constant from that used above T_o. Similarly to the d^1 case, the susceptibility continues to deviate from the Curie-Weiss law below T_o, however, the deviations are smaller and so is the enhancement of the effective magnetic moment due to mixing of the $J = 2$ states with higher energy multiplets. We note that when $J_{\rm SE} = 0$, the magnetic susceptibility continues to give a negative Curie-Weiss constant due to a non-Curie-Weiss susceptibility as in the d^1 case.

For the canted FM phase in Fig. 8(d), the high T fit of the magnetic susceptibility gives a positive Curie constant, indicating that FM interactions dominate at large $\eta = J_H/U$ in d^2 superexchange terms. The divergence of magnetic susceptibility at T_c features a FM phase transition. However a finite susceptibility for $T < T_c$ appears as a result of the canting angle between the parallel magnetic moments on different planes.

FM [100] structure [Fig. 8(e)]: Deviations from the Curie-Weiss law are seen below T_o, and the sign of the Curie-Weiss constant can switch from negative to positive depending on which temperature region is fitted. Unlike the other phases, magnetic order appears at T_c with a first-order transition marked by the jumps in orbital occupancy and susceptibility. This arises from competition between having the most energetically favorable orbital structure at high temperatures and the most energetically favorable magnetic structure at low temperatures.

Size of moment: We compare values of the theoretical moments to those from experiment. Oxygen hybridization results in a Curie moment of $\mu_{\rm eff} = \mathcal{P}_2(2S - L)\mathcal{P}_2 = J(1 - \gamma/2) = \sqrt{6}(1 - \gamma/2)\mu_B$, where $\mathcal{P}_2$ is projection operator to the d^2 multi-orbital Coulomb interaction ground state[16] $J = 2$ (with moment size $|J| = \sqrt{2(2+1)} = \sqrt{6}$), $\mathcal{P}_2 S\mathcal{P}_2 = J/2, \mathcal{P}_2 L\mathcal{P}_2 = J/2$, γ is the effective orbital moment on the transition metal ion after taking into account the oxygen hybridization. Assuming almost half of the moment resides on oxygen (i.e. $\gamma = 0.5$), the calculated moment is then $\mu_{\rm eff} \approx 1.8\mu_B$. This is close to the experimentally observed moments in Sr_2MgOsO_6 and Ca_2MgOsO_6 (both $1.87\mu_B$)[5] but farther off from those of Ba_2YReO_6 ($1.93\mu_B$) [36] and La_2LiReO_6 ($1.97\mu_B$) [36].

[1] W. Witczak-Krempa, G. Chen, Y. B. Kim, and L. Balents, Annual Review of Condensed Matter Physics **5**, 57 (2014).
[2] J. G. Rau, E. K.-H. Lee, and H.-Y. Kee, Annual Review of Condensed Matter Physics **7**, 195 (2016).
[3] H. L. Feng, Y. Shi, Y. Guo, J. Li, A. Sato, Y. Sun, X. Wang, S. Yu, C. I. Sathish, and K. Yamaura, Journal of Solid State Chemistry **201**, 186 (2013).
[4] C. M. Thompson, J. P. Carlo, R. Flacau, T. Aharen, I. A. Leahy, J. R. Pollichemi, T. J. S. Munsie, T. Medina, G. M. Luke, J. Munevar, S. Cheung, T. Goko, Y. J. Uemura, and J. E. Greedan, Journal of Physics: Condensed Matter **26**, 306003 (2014).
[5] Y. Yuan, H. L. Feng, M. P. Ghimire, Y. Matsushita, Y. Tsujimoto, J. He, M. Tanaka, Y. Katsuya, and K. Yamaura, Inorganic Chemistry **54**, 3422 (2015), pMID: 25751088, http://dx.doi.org/10.1021/ic503086a.
[6] R. Morrow, A. E. Taylor, D. J. Singh, J. Xiong, S. Rodan, A. U. B. Wolter, S. Wurmehl, B. Büchner, M. B. Stone, A. I. Kolesnikov, A. A. Aczel, A. D. Christianson, and P. M. Woodward, Scientific Reports **6**, 32462 (2016).
[7] K. E. Stitzer, M. D. Smith, and H.-C. zur Loye, Solid State Sciences **4**, 311 (2002).
[8] C. A. Marjerrison, C. M. Thompson, G. Sala, D. D. Maharaj, E. Kermarrec, Y. Cai, A. M. Hallas, M. N. Wilson, T. J. S. Munsie, G. E. Granroth, R. Flacau, J. E. Greedan, B. D. Gaulin, and G. M. Luke, Inorganic Chemistry **55**, 10701 (2016).
[9] A. S. Erickson, S. Misra, G. J. Miller, R. R. Gupta, Z. Schlesinger, W. A. Harrison, J. M. Kim, and I. R. Fisher, Phys. Rev. Lett. **99**, 016404 (2007).
[10] H. J. Xiang and M.-H. Whangbo, Phys. Rev. B **75**, 052407 (2007).
[11] K.-W. Lee and W. E. Pickett, EPL (Europhysics Letters) **80**, 37008 (2007).
[12] S. Gangopadhyay and W. E. Pickett, Phys. Rev. B **91**, 045133 (2015).
[13] L. Xu, N. A. Bogdanov, A. Princep, P. Fulde, J. v. d. Brink, and L. Hozoi, npj Quantum Materials **1**, 16029 (2016).
[14] K.-H. Ahn, K. Pajskr, K.-W. Lee, and J. Kunes, Phys. Rev. B 95, 064416 **95**, 064416 (2017).
[15] G. Chen, R. Pereira, and L. Balents, Phys. Rev. B **82**, 174440 (2010).
[16] G. Chen and L. Balents, Phys. Rev. B **84**, 094420 (2011).
[17] T. Dodds, T.-P. Choy, and Y. B. Kim, Phys. Rev. B **84**, 104439 (2011).
[18] H. Ishizuka and L. Balents, Phys. Rev. B **90**, 184422 (2014).
[19] J. Romhányi, L. Balents, and G. Jackeli, Phys. Rev. Lett. **118**, 217202 (2017).

[20] A. Georges, L. de' Medici, and J. Mravlje, Annual Review of Condensed Matter Physics **4**, 137 (2013).
[21] G. Khaliullin, Progress of Theoretical Physics Supplement **160**, 155 (2005).
[22] A. Paramekanti, D. J. Singh, B. Yuan, D. Casa, A. Said, Y.-J. Kim, and A. D. Christianson, Phys. Rev. B **97**, 235119 (2018).
[23] A. E. Taylor, S. Calder, R. Morrow, H. L. Feng, M. H. Upton, M. D. Lumsden, K. Yamaura, P. M. Woodward, and A. D. Christianson, Phys. Rev. Lett. **118**, 207202 (2017).
[24] S. V. Streltsov and D. I. Khomskii, Proceedings of the National Academy of Sciences **113**, 10491 (2016), https://www.pnas.org/content/113/38/10491.full.pdf.
[25] See Appendix C for details. We also thank R. Arita for DFT estimates. (Private communication).
[26] Given the uncertainty in estimating V (Appendix C), we have checked that $T_c < T_o$ irrespective of the relative strength of $J_{\rm SE}$ and V.
[27] J. Goodenough, Magnetism and the Chemical Bond (Interscience Publishers, 1963).
[28] J. Kanamori, J. Phys. Chem. Solids **10**, 87 (1959).
[29] P. W. Anderson, Phys. Rev. **115**, 2 (1959).
[30] J. Xiong, J. Yan, A. A. Aczel, and P. Woodward, J. Solid State Chemistry **258**, 762 (2018).
[31] D. Hirai, H. Sagayama, S. Gao, H. Ohsumi, G. Chen, T.-h. Arima, and Z. Hiroi, Phys. Rev. Research **2**, 022063 (2020).
[32] D. Hirai and Z. Hiroi, Journal of Physics: Condensed Matter **33**, 135603 (2021).
[33] L. Lu, M. Song, W. Liu, A. P. Reyes, P. Kuhns, H. O. Lee, I. R. Fisher, and V. F. Mitrović, Nat. Commun. **8**, 14407 (2017).
[34] B. J. Kim and G. Khaliullin, Phys. Rev. B **96**, 085108 (2017).
[35] E. Şaşıoğlu, C. Friedrich, and S. Blügel, Phys. Rev. B **83**, 121101 (2011).
[36] T. Aharen, J. E. Greedan, C. A. Bridges, A. A. Aczel, J. Rodriguez, G. MacDougall, G. M. Luke, V. K. Michaelis, S. Kroeker, C. R. Wiebe, H. Zhou, and L. M. D. Cranswick, Phys. Rev. B **81**, 064436 (2010).